Application and Benchmarking of a Novel Coupled Methodology for Simulating the Thermomechanical Evolution of Sodium-cooled Fast Reactors Fuel Subassemblies

Francisco Acosta, Pablo Rubiolo, Victor Blanc, Thierry Cadiou

Version of Record: https://www.sciencedirect.com/science/article/pii/S0029549320305422
Manuscript_d1ac81941a70f85dc42cd65dab955077

SIMULATING THE THERMOMECHANICAL EVOLUTION OF SFR FUEL SUBASSEMBLIES WITH A NOVEL COUPLED APPROACH

Acosta Francisco[1,*], Rubiolo Pablo[2], Blanc Victor[3], Cadiou Thierry[1]

[1] CEA, DEN, DER, SESI*, 13108*, Saint Paul lez Durance, France

[2] Professor, University of Grenoble-Alpes, CNRS/IN2P3, 38000, Grenoble, France

[3] CEA, DEN, DEC, SESC, *13108,* Saint Paul lez Durance, France

**Present address: 1*0 Rue Juliette Récamier, 69006 Lyon, France (francisco.acosta@framatome.com)

ABSTRACT

We employ a novel methodology to simulate the irradiation of Sodium cooled Fast Reactors (SFR) subassemblies. The proposed approach allows considering the coupling between key thermal-hydraulic and thermomechanical phenomena, which is usually neglected in traditional simulation methods. Comparisons between results obtained from coupled and uncoupled methodologies show that the latter can significantly over predict the stresses and the strains of highly irradiated fuel bundles. Additionally, we explore different options for the pin mechanical modeling. In particular, we show that a relatively simple beam-based finite element model for the fuel pins can be used to efficiently compute swelling and irradiation creep strains averaged over the cross section of the fuel claddings. However, if a prediction of the cladding swelling gradients is needed, the beam model must be replaced by a more computationally expensive 3D fuel pin model. An efficient method to estimate the fuel cladding temperature evolution based on a limited number of Computational Fluid Dynamic (CFD) simulations is also presented in this work, and its performance is evaluated. Finally, a numerical benchmark against the state-of-the-art coupled code system for the simulation of SFR subassemblies is presented. This benchmark shows that the proposed coupled methodology allows obtaining results that are in good agreement with the reference methodology. However, two clear advantages of the proposed methodology were identified. Firstly, the use of detailed CFD simulations in our methodology, compared to the lower resolution thermal-hydraulic model employed in the state-of-the-art approach. Secondly, considering the reduction of the coolant mass flow rate caused by the fuel bundle deformation, neglected in the pre-existing approach, which is shown in this work to have a potentially large impact on the coolant temperature distribution.

1 INTRODUCTION

During their irradiation in the core of SFR, the wire-wrapped fuel pin claddings and the hexagonal wrapper tubes that constitute their subassemblies undergo severe geometrical changes under the effects of void swelling and irradiation creep [1]. These phenomena are temperature dependent [2][3] and thus require an accurate fuel pin thermal model. Moreover, during irradiation, the resulting fuel bundle deformation induces local temperature perturbations and increases the fuel pin hydraulic resistance, which leads to a significant reduction of the coolant mass flow rate and to a cladding temperature increase. Therefore, since the deformation mechanisms both depend on and affect the fuel pin temperature distribution, it results that the thermal-hydraulic and thermomechanical evolution of SFR subassemblies under irradiation are coupled.

Traditionally, this coupling has been neglected in the numerical simulations since the temperature distribution used as input for the thermomechanical calculations is often determined from thermal-hydraulic simulations using the reference (non-deformed) fuel assembly geometry and low-resolution subchannel codes. In order to improve the accuracy of the subassembly deformation calculations, a new coupled simulation methodology has been developed at the French Alternative Energies and Atomic Energy Commission (CEA) [4]. This new methodology is based on the coupling of a Reynolds Averaged Navier Stokes (RANS) thermal-hydraulics model developed in the CFD code STAR-CCM+ [5] and the in-house SFR bundle thermomechanical code DOMAJEUR2.

In this work, we illustrate the interest of applying the coupled methodology to study the behavior of SFR subassemblies under irradiation, from the perspective of the mechanical integrity of the fuel pins during nominal reactor operation. The present analysis is focused on the coupling effects on strains and stresses, and on the capability of the CFD RANS model to resolve the high temperature gradients in the fuel pin claddings, which also have consequences on their mechanical integrity. Additionally, we introduce and evaluate the performance of a novel method for predicting the evolution of the cladding temperature distribution during the irradiation. Finally, we compare the predictions of the proposed coupled methodology with the state-of-the-art coupled code system for the simulation of the irradiation of SFR subassemblies.

This paper is organized as follows. In Section 2, we introduce the main physical phenomena involved in the evolution of SFR subassemblies under irradiation, the deformation mechanisms that they induce and the thermomechanical models typically used to simulate their irradiation. Then, in Section 3, we describe the proposed coupled methodology and the thermomechanical models employed, which have been described in detail in a previous work [4]. In this paper, however, we introduce a new model which allows to improve the prediction of the evolution of the cladding temperature distribution, with respect to the model presented in [4], while limiting the number of required CFD simulations, and thus the computational cost. An application example of the coupled methodology is presented in Section 4, where the effects of considering the coupling in the numerical simulations of highly irradiated fuel bundles are evaluated, while the performance of the new temperature prediction model is evaluated in Section 5. Finally, a numerical benchmark is presented in Section 6, where we compare the results obtained with STAR-CCM+/DOMAJEUR2 to those obtained with the coupling ASFRE/BAMBOO [6], which

represents the state-of-the art in the simulation of SFR subassemblies. The conclusions of this work are given in Section 7.

2 THERMOMECHANICAL EVOLUTION OF SFR SUBASSEMBLIES UNDER IRRADIATION

2.1 PHENOMENA INVOLVED IN THE EVOLUTION OF THE SFR SUBASSEMBLIES

In nominal operation conditions, the main causes of the deformation of SFR subassemblies are void swelling and irradiation induced creep. Void swelling can be defined as the isotropic volume increase caused by the coalescence and growth of voids within the material, consequence of the irradiation induced mobile defects. It is characterized by having an incubation period during which the volume change remains relatively small, despite the increasing irradiation dose [7]. After a certain incubation dose is reached, the swelling rate grows until attaining a steady state value. The volume swelling rate per dpa (Displacement Per Atom), $\dot{g}$, can be written as a function of the irradiation dose D in the form given by Equation 1 below:

$$\dot{g} = \frac{\dot{g_0}}{1+e^{\left(\frac{\Delta g - D}{\delta g}\right)}} \tag{1}$$

where $\dot{g_0}$ is the steady state swelling rate per dpa (i.e. units are [1/dpa]), Δ_g the incubation dose, and δ_g the transition dose from incubation to steady state. Due to its isotropy, the swelling strain $\varepsilon_{swelling}$ can be expressed as:

$$\varepsilon_{swelling} = (1+g)^{1/3} - 1 \tag{2}$$

Both the incubation dose and the steady state swelling rate depend on the material temperature. Swelling affects mainly the fuel claddings and spacer wires, since the martensitic alloys employed for the hexagonal wrapper tube—also called hexcan—show an excellent swelling stability [8].

The irradiation damage greatly enhances the mobility of crystallographic defects such as vacancies, interstitials, and dislocations, which gives place to a phenomenon called irradiation creep, which can be defined as the isochoric irreversible strain of a material under the effect of stresses. At low temperature, irradiation creep can be orders of magnitude higher than thermally induced creep and therefore it is the dominant creep mechanism [7][9]. The irradiation creep equivalent strain rate $\dot{\varepsilon}_{eq}^{irr.\ creep}$ (with units [1/dpa]) can be expressed as a function of the equivalent stress σ_{eq} and the volume swelling rate as indicated by Equation 3:

$$\dot{\varepsilon}_{eq}^{irr.\ creep} = \left(1 + 2\alpha\sigma_{eq}\right)K\sigma_{eq} + \alpha\sigma_{eq}\dot{g} \tag{3}$$

where K is the temperature dependent creep compliance parameter, and α the creep swelling coupling coefficient that is considered to take a constant positive value.

For the reference cladding austenitic steel of French SFR, the steady state swelling strain rate and the irradiation creep $\dot{\varepsilon}_{eq}^{irr.\ creep}$ are maximal in the temperatures from 485°C to 525°C, as can be seen in Figure 1a. At higher temperatures, they both have negative partial derivatives with respect to temperature ($\partial\varepsilon/\partial T$). The swelling incubation dose increases monotonically with temperature up to about 750°C, which shifts the maximum integrated swelling to slightly lower temperatures (~450°C-490°C), as can be observed in Figure 1b.

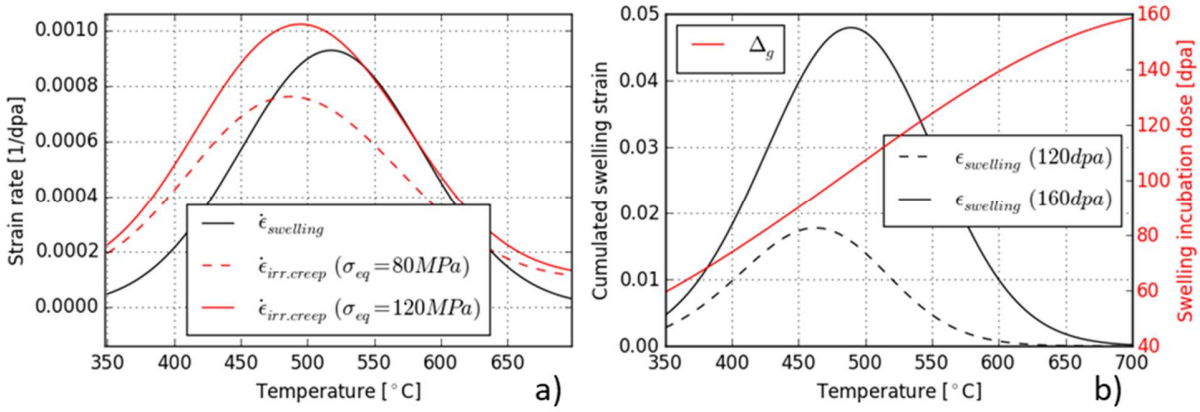

Figure 1: Temperature dependence of swelling steady state strain rate and irradiation creep rate for different equivalent stress σ_{eq} (a), and of the incubation dose and cumulated swelling strain for different irradiation doses (b).

2.2 SFR Bundle Deformation Mechanisms and Mechanical Design Criteria

The high fast neutron flux to which the cladding of the fuel pins are exposed, added to the high temperatures and increasing internal fission gas pressure during their irradiation, activate the aforementioned swelling and irradiation creep. These phenomena lead to a significant strain of the claddings and their spacer wires, which are also subject to thermal expansion. Macroscopically, these strains lead to the bowing of the fuel pins, their helical flexion, the increase in the diameter of the claddings and the wires, and their ovalization [1], [10].

The fuel assembly deformation as result of the irradiation damage can be divided in three phases according to the bundle interaction. The bowing appears in the first phase, from the beginning of the irradiation, and it is caused by the differential thermal expansion of the claddings. The associated stresses are low since the bowing involves the entire length of the fuel pins. As the irradiation proceeds, the differential deformation of each cladding and the spacer wire around it leads to the helical flexion of the pin under the tension of the wire. The contact between fuel pins through the spacer wires, which occurs during normal operation, marks the start of the 2^{nd} phase of bundle interaction, illustrated in Figure 2a. The forces caused by the contact increase the pin helical flexion, which helps to accommodate its growing diametral strain. If the irradiation continues, a time comes where the pins cannot continue

flexing and the ovalization of the claddings is the only mechanism available to mitigate the mechanical interaction between pins. This is called 3^{rd} phase of bundle interaction, illustrated in Figure 2b, and is not allowed in normal operation since, with the typical SFR fuel pin geometry, higher forces are required for the ovalization of the cladding than for its flexion following the wire step.

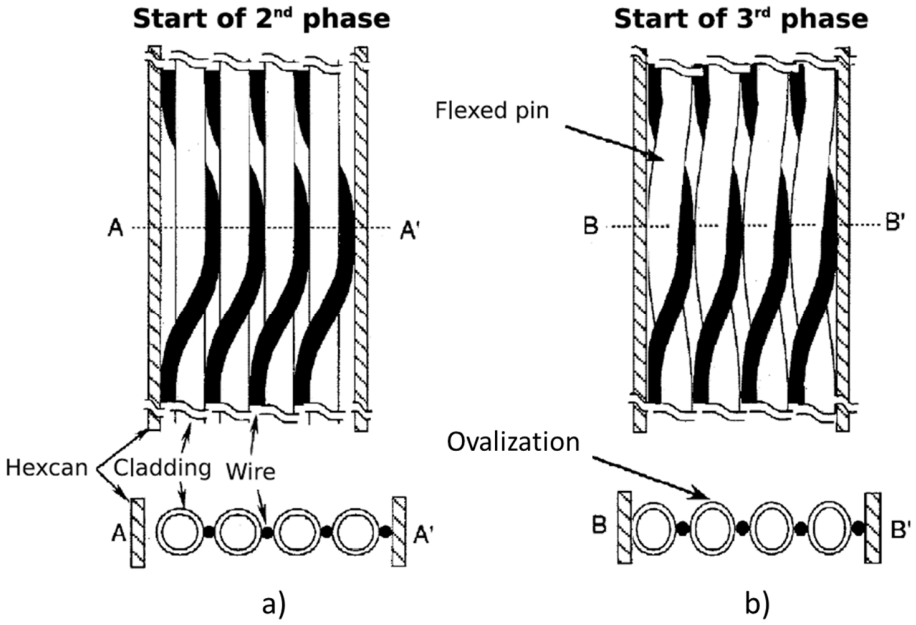

Figure 2: Schematic representation of the start of the 2^{nd} (a) and 3^{rd} (b) phases of interaction between the fuel pins, and between the pins and the hexcan. Adapted from [11].

Since the cladding of the fuel pins constitutes the first containment barrier for the nuclear fuel material, and its failure would release radioactive isotopes into the primary circuit, a set of design criteria have been developed to guarantee their physical integrity [12]. Table 1 summarizes the most relevant mechanical design criteria and the failure mechanism each of them addresses. The limiting values presented here are similar between the different SFR development programs around the world.

Criteria	Limiting value	Associated undesired effect
Maximum equivalent stress	< yield point	Plastic instability
Pin diametral increase	< 7%	Insufficient cooling + 3^{rd} phase of bundle mechanical interaction
Cladding volume swelling	< 6%	Embrittlement of austenitic steel
Cumulative creep-rupture damage factor (CDF)	< 0.2-0.3	Creep rupture under the effect of internal pressure
Cladding thermal creep strain	< 0.2%	Creep rupture

Table 1: Typical mechanical design criteria of SFR fuel bundles.

2.3 TYPICAL THERMOMECHANICAL MODELS EMPLOYED TO VERIFY THE DESIGN CRITERIA

A key part of the design process of the SFR fuel subassemblies consists in conducting numerical simulations to verify that the design criteria are respected during nominal operation and in some accidental scenarios. A widely adopted approach relies on the use of finite element methods to model the thermomechanical evolution of one isolated fuel pin, including the cladding and the fuel pellets it contains, as well as the pellet cladding interaction. Such simulations are typically conducted with a so-called 1D1/2 axisymmetric representation of the fuel pin, which is divided into several axial slices. In each slice, the heat transfer from the cladding to the sodium is also solved for, and adjacent slices are coupled by the heat transported by the coolant. This modelling strategy is employed, for example, in the fuel performance code GERMINAL of the CEA [13].

A different kind of approach exists to model the entire fuel bundle, in order to include the effects of the mechanical interactions between fuel pins, and between pins and the hexcan. To avoid an excessively high computational cost, in this approach, the mechanical interactions between the fuel pellets and the cladding, usually very limited during normal operation [14], are neglected. Additionally, the mesh employed in these numerical simulations is either courser than the previous or they a relatively simple beam-based representation of the bundle. Examples of this are the BAMBOO code [15], and the bundle thermomechanical code DOMAJEUR2, developed by the CEA and used in the present work.

In DOMAJEUR2, which is based on the finite element analysis code CAST3M [16], the quasi-static thermomechanical evolution of the fuel pin claddings, the spacer wires, and the hexcan is modeled by a finite element representation. The effects of void swelling, and irradiation and thermal creep under the action of the internal fission gas pressure are considered by means of experimentally determined laws. The thermal expansion of the materials and the contacts between fuel pins and between the pins and the hexcan are also considered in the analysis. To explore different modeling strategies, models with different geometrical representations (described in Section 3.3) are available in DOMAJEUR2, ranging from a fully 3D model that employs volumetric finite elements to a beam-based model.

3 NEW COUPLED METHODOLOGY FOR THE SIMULATION OF SFR SUBASSEMBLIES

3.1 IMPLEMENTED COUPLING

Traditionally, the temperature distribution of the fuel pin claddings—one of the main inputs for the thermomechanical simulations—is computed with low resolution codes (e.g. subchannel codes) in a geometry with as-fabricated dimensions, and it is assumed constant during the irradiation. Recently, however, a new simulation approach has been presented by [6], in which the bundle thermomechanics code BAMBOO is coupled with the thermal-hydraulic subchannel code ASFRE [17], following the operator split coupling paradigm. Although this approach represents an advance in the simulation of SFR subassemblies, it has some important limitations. The first one is the use of a low-resolution thermal-

hydraulic code, which relies on empirical correlations to compute the cross flow between the different subchannels. Indeed, this type of thermal hydraulic model has been shown to perform poorly when compared to currently available CFD techniques [18], especially in significantly deformed fuel bundles [19]. Additionally, the effect of the deformation on the fuel assembly coolant mass flow rate is not considered in this approach, even though the authors acknowledge the existence of this phenomena. As we will show in this work, this effect is can be significant.

On the other hand, the methodology simulation employed in this paper, firstly introduced in [4], is based on the numerical coupling between a detailed RANS model of SFR subassemblies, implemented in the CFD code STAR-CCM+, and a SFR bundle thermomechanical model using the code DOMAJEUR2 (CEA inhouse code). In this novel approach, the cladding temperature distribution is computed by means of a detailed RANS model in which the diametral strain and the helical flexion of the claddings can be explicitly considered to compute the temperature field in the deformed geometry. Moreover, a dedicated thermal-hydraulics model ([4], [20]) allows to calculate the sodium mass flow rate reduction caused by the bundle deformation and thus modify accordingly the boundary condition of the CFD simulations.

In order to calculate the time evolution of the strain and stress distributions within the fuel pin bundle, DOMAJEUR2 requires the evolution over time of the cladding temperature distribution, $T(r,t)$. The straightforward approach consisting in performing thermal-mechanics and thermal-hydraulics (CFD) fully coupled simulations (i.e. in each time step thermal-mechanics and thermal-hydraulics simulations are performed and the temperature and deformation fields are exchanged) is not practical because of the computation cost of the CFD calculation. Instead, as discussed in the next section, we employ an alternative approach based on a very limited number of CFD calculation and the use of an efficient extrapolation strategy to estimate the cladding temperature evolution for the thermal-mechanics simulations.

3.2 TIME HISTORY OF THE CLADDING TEMPERATURE DISTRIBUTION

As described in the previous section, the cladding temperature time history is computed based on the interpolation of temperature fields obtained with CFD simulations in deformed geometries at different time steps of the thermomechanical simulation. Conducting one CFD simulation in the geometry computed at every time step of the thermomechanical simulation would be equivalent to the traditional operation split coupling technique, which is to this day, and mainly due to the simplicity of its implementation, the paradigm in multiphysical coupling [21]. However, performing such a large number of CFD simulations would imply an extremely high computational cost, which is why the aim of the methodology here presented is to reduce as much as possible the number of required CFD simulations, while correctly capturing the coupling between the cladding temperature increase and the temperature-dependent cladding deformation mechanisms. To this end, different strategies to estimate $T(r,t)$ are here considered, and they are illustrated in Figure 3 for a material point r_0 within the cladding of a subassembly with constant power.

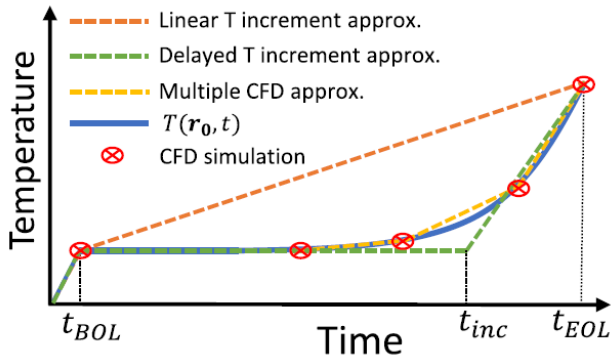

Figure 3: Schematic representation of a typical fuel cladding temperature time evolution $T(r_0, t)$, at constant subassembly power, and of different approximating functions.

The temperature evolution $T(r_0, t)$ observed in Figure 3 is a consequence of the incubation period of the cladding swelling and, later on, to its exponential transition towards a constant swelling rate (see Section 2.1). The simplest approximation of $T(r_0, t)$ consists in considering a linear temperature increment between a time t_{BOL} at the beginning of life (BOL) and the end of irradiation, t_{EOL}. Alternatively, the incubation period can be explicitly considered by assuming that no deformation-induced temperature change occurs until a time t_{inc}, from which the temperature is considered to increase linearly with time. This approach is illustrated in Figure 3 and is called here *Delayed T increment approximation*. Both approximations make use of only two CFD-computed temperature distributions, one of which is the EOL temperature distribution. Finally, one could also interpolate the temperature distribution based on multiple CFD calculations, each of them in a different deformed geometry as computed by the thermomechanical code for different instants during the irradiation.

With the *Delayed T increment approximation*, the cladding temperature history $\tilde{T}^k(\boldsymbol{r}, t)$ computed in an iteration k, and then used as input for a thermomechanical simulation, is given by Equation 4 below:

$$\tilde{T}^k(\boldsymbol{r}, t) =$$

$$\begin{cases} T_{cold} + \frac{t}{t_{BOL}}(T(\boldsymbol{r}, t_{BOL}) - T_{cold}),\ for\ 0 \le t \le t_{BOL}\ (Startup) \\ T(\boldsymbol{r}, t_{BOL}) + \frac{t - t_{BOL}}{t_{EOL} - t_{BOL}}\left(T_{Nom}(\boldsymbol{r}, t_{EOL}) - T(\boldsymbol{r}, t_{BOL})\right),\ for\ t_{BOL} < t \le t_{inc}^k\ (Incubation) \\ \tilde{T}^k\left(\boldsymbol{r}, t_{inc}^k\right) + \frac{t - t_{inc}^k}{t_{EOL} - t_{inc}^k}\left(T^k(\boldsymbol{r}, t_{EOL}) - \tilde{T}^k\left(\boldsymbol{r}, t_{inc}^k\right)\right),\ for\ t_{inc}^k < t \le t_{EOL}\ (Deformation) \end{cases}$$

(4)

Between $t = 0$ and BOL, $t_{BOL} = 1$ Full Power Day (FPD), a linear temperature evolution from an isothermal state T_{cold} to $T(\boldsymbol{r}, t_{BOL})$ is considered, where $T(\boldsymbol{r}, t_{BOL})$ is computed with a CFD simulation in the nominal (non-deformed) geometry and with the BOL power distribution. From t_{BOL} until t_{inc}^k, the temperature is assumed to evolve linearly as a consequence of the variation of the subassembly power with its burn-up. This linear evolution is computed by interpolating between $T(\boldsymbol{r}, t_{BOL})$ and $T_{Nom}(\boldsymbol{r}, t_{EOL})$, which is the temperature distribution obtained in the nominal geometry but with the

EOL power distribution (therefore it does not depend on the deformation level). Finally, between t_{inc}^{k} and the end of the irradiation, t_{EOL}, a linear evolution between $\tilde{T}^{k}(\boldsymbol{r}, t_{inc}^{k})$ and $T^{k}(\boldsymbol{r}, t_{EOL})$ is considered, where $T^{k}(\boldsymbol{r}, t_{EOL})$ is obtained with a CFD simulation in the last computed EOL deformed geometry and with EOL boundary conditions, including the power level and the last computed mass flow rate which depends on the deformation of the fuel bundle. Then, to construct this temperature history, three CFD simulations are required for the first iteration if the subassembly power evolves with time—two of which, $T(\boldsymbol{r}, t_{BOL})$ and $T_{Nom}(\boldsymbol{r}, t_{EOL})$, are conducted in the same non-deformed geometry—, while only 2 are needed if the power is constant, like in the example presented in Figure 3. In both scenarios, one CFD simulation per additional iteration is required.

To define $\tilde{T}^{k}(\boldsymbol{r}, t)$, the time t_{inc}^{k} from which the effects of the deformation on temperature are considered still needs to be determined. In order to do so, the last computed evolution of the creep and swelling induced diametral strain of each fuel pin p at the axial position of maximal EOL deformation, $\varepsilon_{Max,p}^{k-1}(t)$, is considered. The choice of this variable is motivated by considering that the diametral strain of the claddings is the leading cause of the coolant mass flow rate reduction in a deformed fuel bundle which, in turn, has a preponderant role in the subsequent cladding temperature increase. By summing over all the fuel pins p we define:

$$\varepsilon_{Max}^{k-1}(t) = \sum_{p} \varepsilon_{Max,p}^{k-1}(t) \tag{5}$$

Then, we consider the following piecewise linear approximate function $\tilde{\varepsilon}_{Max}^{k-1}(t)$ that has a break at a time t_{inc}^{k}, which is its only free parameter:

$$\tilde{\varepsilon}_{Max}^{k-1}(t) = \begin{cases} 0, & for\ t < t_{inc}^{k} \\ \varepsilon_{Max}^{k-1}(t_{EOL}) \frac{t - t_{inc}^{k}}{t_{EOL} - t_{inc}^{k}}, & for\ t \leq t_{inc}^{k} \leq t_{EOL} \end{cases} \tag{6}$$

Finally, the value of t_{inc}^{k} is determined, for an iteration k, by fitting $\tilde{\varepsilon}_{Max}^{k-1}(t)$ to the $\varepsilon_{Max}^{k-1}(t)$ calculated in the thermomechanical simulation of the previous iteration. The least squares method is employed for the fitting, an example of which is illustrated in Figure 4.

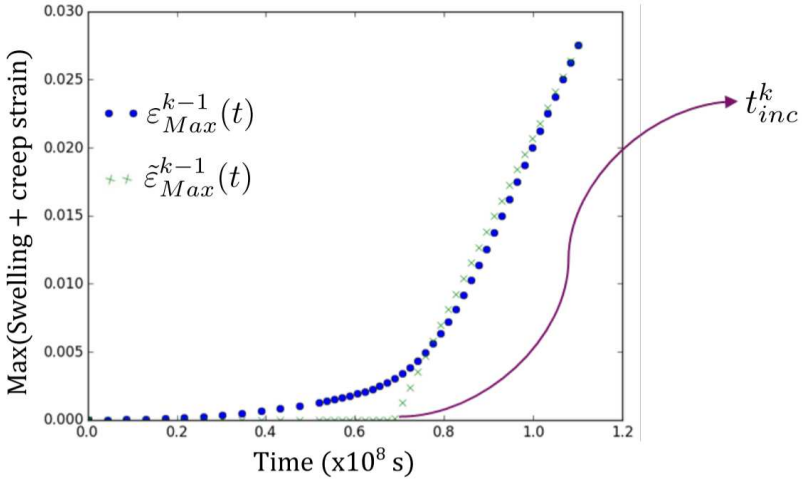

Figure 4: Example of the fitting of $\varepsilon_{Max}^{k-1}(t)$ employed to determine t_{inc}^{k}.

In Section 5, the performance of the *Delayed T increment approximation* is evaluated, and it is there compared with the other approaches mentioned in this section, illustrated in *Figure 3*.

3.3 THERMOMECHANICAL MODELS EMPLOYED

Two different models available in DOMAJEUR2, described in detail in [4], are employed in this work. The first one uses volumetric finite elements to represent the fuel claddings and the hexcan, while the wires are represented by beam elements. The potential contact points between adjacent fuel pin claddings and between claddings and the hexcan, consequence of the bundle deformation, are linked by elastic gap elements. Before contact occurs, they have almost null stiffness, which takes an extremely high value when these elements are activated by the contact. The nonlinear viscoplastic nature of the crushing of the claddings is thus represented by the models of the volumetric finite elements that constitute them.

The second model here employed relies on special 1D hollow beam finite elements, which allow considering the effects of an internal pressurization, to represent the fuel claddings, while shell elements are used for the hexcan. The potential contact points mentioned before are linked by beam finite elements that include an *ad hoc* model to estimate the stress and strain state of the cladding at its internal radius in the positions where contact occurs [9]. This is the point more susceptible to being damaged by thermal creep and, since it has a high order dependence on the stress, a very high accuracy is required to properly compute it. The 3D model evoked above could be employed to this end, but the mesh refinement required for the simulation of entire SFR fuel bundles is currently prohibitive in terms of computational power. It is precisely to overcome this limitation that the special beam element has been developed.

The 1D model of the contact elements describes the elasto-viscoplastic crushing of the cladding under the contact between fuel pins, and between the pins and the hexcan. It considers the effects of thermal expansion, swelling, creep, and the modification of the structural rigidity of the cross section of the cladding due to its ovalization. Under these conditions, the model computes the strain and stress tensor in the inner radius on the cladding by means of stress and strain concentration factors, which depend on the ovalization and are determined with very detailed elastic finite element simulations of the crushing of a fuel cladding [9].

As it will become apparent later, it is important to highlight that only the 3D model is currently capable of considering the high temperature gradients that the claddings are subject to.

4 APPLICATION CASE

4.1 IRRADIATION OF A 7-PIN SFR FUEL BUNDLE. CASE DESCRIPTION

In this work, we firstly analyze the evolution of a 7-pin fuel bundle irradiated to up to a maximal dose of 165 dpa (close to the maximum dose reached by a subassembly of the PHENIX reactor[1] [23]) with characteristic dimensions and boundary conditions, presented in Table 2, representative of a 4th generation SFR design [8]. One of these characteristics is the fertile blanket in the central region of the heated column, the effect of which can be observed in the irradiation dose and linear power profiles employed for the simulations conducted here, presented in Figure 5 along with the cross section of the bundle and the pin naming system. In this figure, as in the rest of this paper, the axial position is measured from the start of the heated column.

Parameter	Value
Fuel pin length	2.136 m
Heated column length	0.8 m (From an altitude of 1.261 m to 2.061 m)
Fuel pin pitch	10.8 mm
Fuel pin external diameter	9.7 mm
Spacer wire diameter	1.0 mm
Spacer wire helix step	180 mm
Maximum linear power	550 W/cm
Mass flow rate in nominal conditions	1.2 kg/s
Inlet sodium temperature	400 °C
Hexcan plate to plate distance	30.6 mm

Table 2: Key geometrical and thermal-hydraulic parameters of the simulated 7-pin bundle.

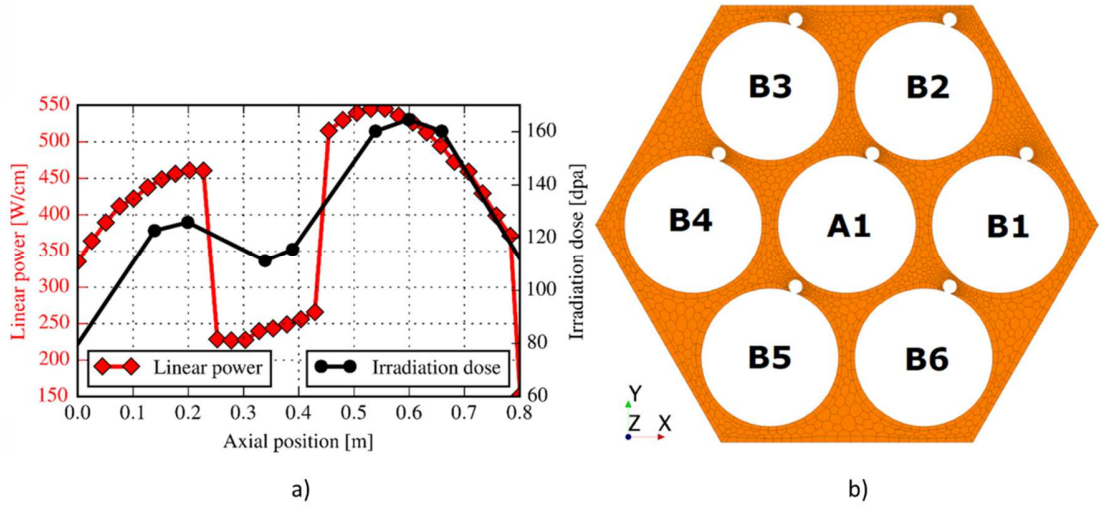

Figure 5: Axial profiles of linear power and irradiation dose employed in the numerical simulations of the 7-pin fuel bundle. b) Cross section of the CFD mesh at the outlet of the 7-pin bundle, where the pin naming system is indicated.

[1] SFR operated in France from 1973 to 2009

The 3D and the beam-based thermomechanical models were employed to conduct coupled simulations of the subassembly. In the 3D model, every cladding is subdivided in 144 axial slices, each of which is represented with a combination of 13 cubic and prismatic elements (1 element in the cladding thickness) with quadratic basis functions. In the 1D model, each pin cladding is represented by 144 beam elements. The total number of elements used for the fuel pins and the hexcan with the 3D and 1D models are 18447 and 4433, respectively, and 860 contact elements are used in both cases. The whole length of the fuel bundle is simulated with DOMAJEUR2, while only the heated column, where the irradiation dose is high enough to induce significant deformation, is represented in the CFD model using over 2 million cells. For this first application example, a linear temperature evolution was considered between BOL and EOL since, as we will show in Section 5, this approach provides a bounding estimation of the impact of the deformation on the temperature distribution.

4.2 Coupling Effects on Swelling and Creep Strains: Full 3D vs Beam-based Finite Elements

The use of a CFD RANS approach allows capturing the complex sodium flow patterns produced by the SFR bundle geometry, including the local effects caused by the spacer wires. This is illustrated in Figure 6, where the computed cladding temperatures for six different azimuthal angles are presented for the central pin A1 (a) and a peripheral pin, B2 (b), in the non-deformed geometry, along the length of their heated columns. Each profile results from averaging, at each axial position, the computed temperatures over one sixth of the circumference of the cladding. This post-processing performed for each CFD simulation in order to generate the temperature evolution used by DOMAJEUR2.

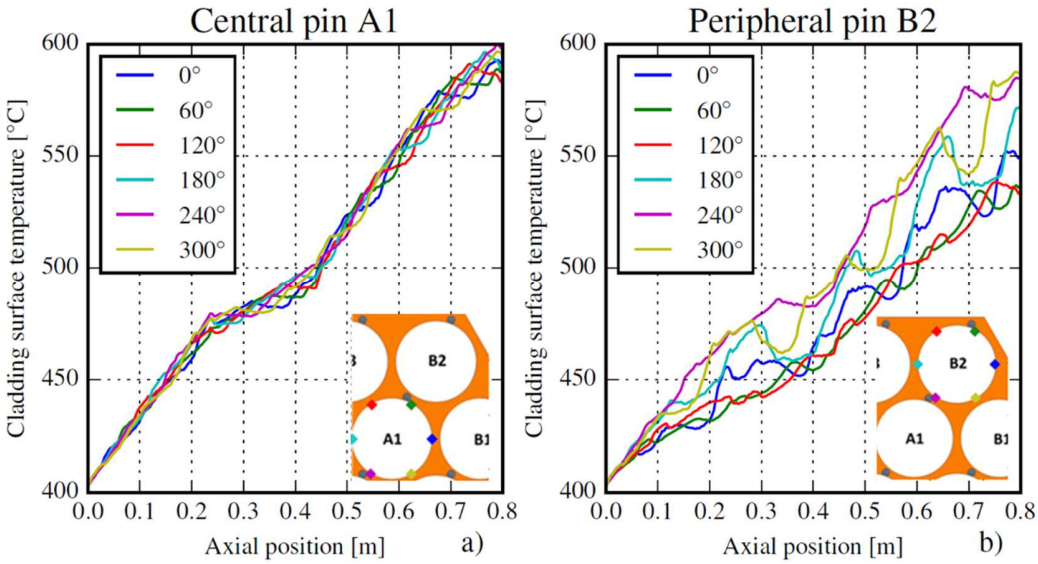

Figure 6: Cladding surface temperature distribution of the central (a) and a peripheral (b) pin in the non-deformed geometry. Each profile corresponds to a different azimuthal angle.

In the deformed bundle, the increased hydraulic resistance reduces the coolant mass flow rate, leading to an overall temperature increase. In addition, the local hydraulic diameter reduction caused by

the cladding diametral strain is more penalizing for the central than for the peripheral subchannels, which are larger. A previous work shows that, when these factors are taken into account in the coupled simulations, the sodium outlet temperature of this 7-pin bundle increases by 30°C, and the temperature gradients of the peripheral pins by about 50% [4]. As can be seen in Figure 6 for the nominal geometry, these gradients are more significant for the peripheral pin since, contrary to the central pin, it is facing the colder hexcan, on one side, and the hotter central subchannels, on the other.

In the cladding temperature range of the upper part of the heated column ($T > 490°C$), we have $\partial\varepsilon/\partial T < 0$ for both $\varepsilon_{swelling}$ and $\varepsilon_{irr\ creep}$ (see Section 2.1). Therefore, the temperature increase induced by the bundle deformation acts as a negative feedback on swelling and creep strains. This can be seen in Figure 7 and in Figure 8, where the EOL swelling strain and the creep hoop strain, averaged over the cross section of the claddings, are presented for the central pin A1 and for the peripheral pin B2, as computed by a non-coupled and a coupled simulation. The results obtained with the DOMAJEUR2 model that employs volume finite elements (3D) as well as with the beam-based model (1D) are presented. In the 3D model, the six temperature profiles obtained for each fuel pin with the CFD simulations are employed to interpolate the temperature, at each axial position, over the 13 elements within the cladding's cross section. On the beam-based model, however, only one average temperature per axial position can be considered.

As can be observed these figures, the axially heterogeneous fuel pin concept, which includes a central fertile blanket, leads to swelling and irradiation creep profiles with two distinct maxima each. In the lower part of the heated column, the irradiation creep strain is dominant, while the contrary is true for the upper part. Additionally, the deformation of the peripheral fuel pin is superior to that of the central pin due to its lower temperature that, in the upper half of the heated column, favors both swelling and irradiation creep.

Concerning the effects of the coupling, it can be noted that they affect the swelling more than the creep strain, and that their impact is maximal for the central pin (Figure 7a), where the swelling strain reduction reaches 30%. The strain reduction due to the coupling is higher in the upper part of the heated column, where the temperature increase induced by the deformation and $\|\partial\varepsilon/\partial T\|$ are both higher.

Additionally, the swelling and creep strains obtained with the beam-based model are in very good agreement with the strains computed by the 3D model (averaged over the cross section of the cladding), despite the fact that only the 3D model considers the azimuthal temperature gradients. In particular, the beam model predicts very well the maximal swelling and creep strains averaged over the circumference of the claddings, which are the main contributors to its diametral strain. This is particularly important since the diametral strain of the cladding induces the other bundle deformation mechanisms described before, leading to the mechanical contact between the fuel pins. The stresses associated to the mechanical contacts might compromise the integrity of the claddings and are thus evaluated next.

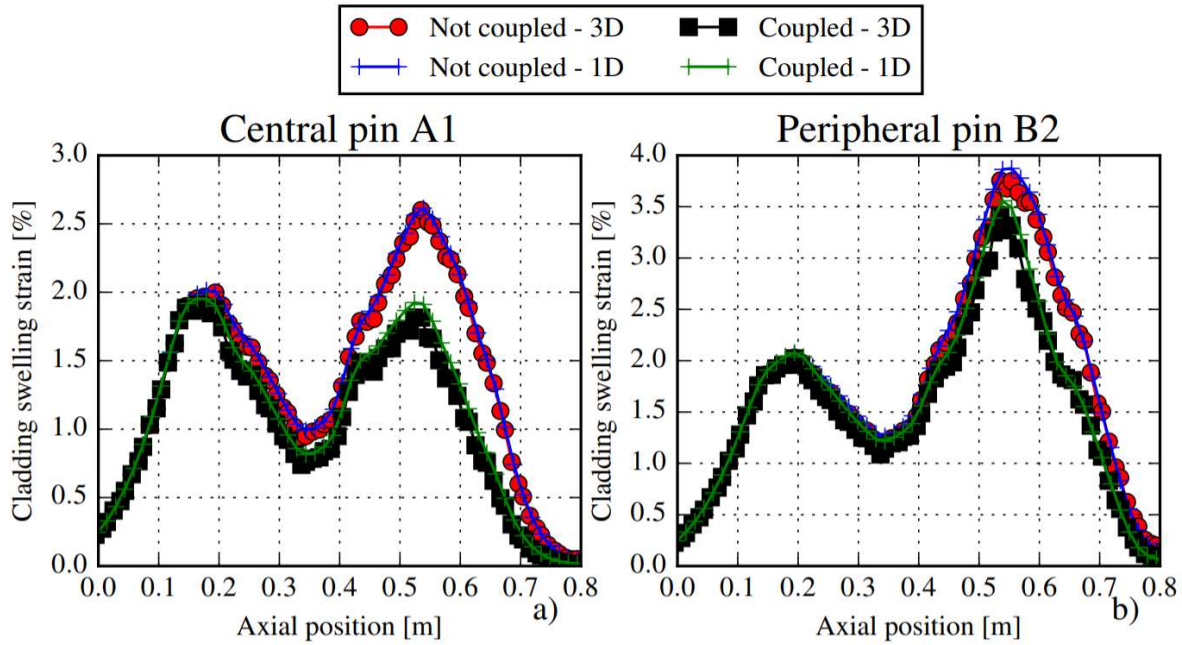

Figure 7: EOL axial average swelling strain profiles of the central (a) and a peripheral pin (b), computed with the 1D and the 3D finite elements models with and without coupling.

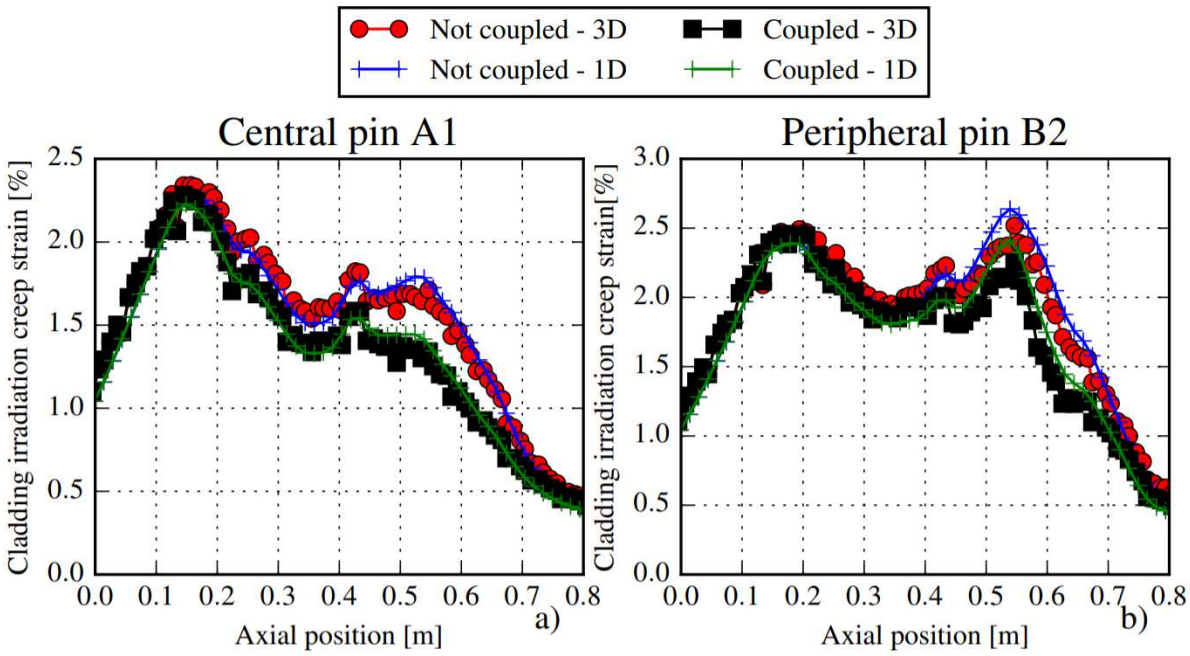

Figure 8: EOL axial average creep strain profiles of the central (a) and a peripheral pin (b), computed with the 1D and the 3D finite elements models with and without coupling.

4.3 COUPLING EFFECTS ON THE STRESS STATE OF THE CLADDINGS

We showed that considering the temperature perturbations induced by the deformation leads to a reduction of the computed swelling and irradiation creep of the claddings, thus to a reduction of their diametral strain. Since the latter is the driving force for the mechanical interactions between fuel pins and between pins and the hexcan, the predicted mechanical loads of these contacts are also reduced in the coupled simulations with respect to the simulations using the non-coupled approach.

To illustrate this, the equivalent von Mises stress calculated by the contact elements, with and without coupling, are presented in Figure 9 for the central pin (a) and a peripheral pin (b). The coupling leads to a substantial reduction of the maximal equivalent stress (~-35% for the central pin), located at the axial position of highest diametral strain. At this axial position, the computed time evolution of the equivalent stress is presented in Figure 10 for the central pin and in Figure 11 for a peripheral pin, along with the evolution of the total available gap (TAG). The TAG is defined, for each diagonal of the hexagonal subassembly, as the difference between the available space within the hexcan and the space occupied by the deformed fuel pins in the diagonal, computed from the average external diameter of their claddings and spacer wires. By definition, the TAG becomes null when contact through the spacer wires starts, which marks the beginning of the 2^{nd} phase of bundle interaction, and $TAG \approx -D_w$ (where D_w is the diameter of the spacer wires) indicates the start of the 3^{rd} phase. The second limit depends on the strain of the hexcan and of the spacer wires, and thus varies slightly during the irradiation as can be observed these figures.

By analyzing Figure 10 and Figure 11, the EOL stress reduction computed with the coupled calculations can be explained by a delay of the 3^{rd} phase of bundle interaction, in which only the cladding's ovalization can accommodate its increasing diametral strain. The start of this phase is characterized by a rapid increase in the equivalent stress, observed at approximately 1540 days in the non-coupled simulation. In the coupled simulation, this phase—which is not allowed in nominal operation—is not reached within the irradiation period considered. Additionally, the first contact-induced stress increase, observed between 1200 and 1300 days, is also delayed by the coupling. It should be noted that, for the central pin, this stress increase appears later than the start of the 2^{nd} phase ($TAG = 0$). This is because, in this fuel bundle, the 2^{nd} phase starts with the contact between the hexcan and a peripheral pin, which interacts with the central pin later on.

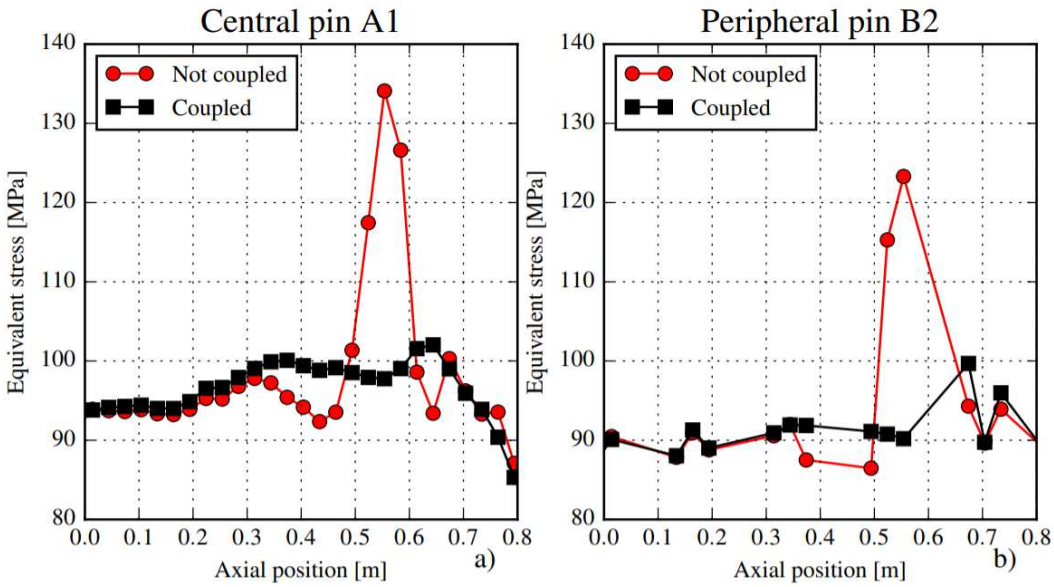

Figure 9: Axial profile of the equivalent stress predicted by the 1D DOMAJEUR2 model, for the central pin A1 (a), and for the peripheral pin B2 (b)

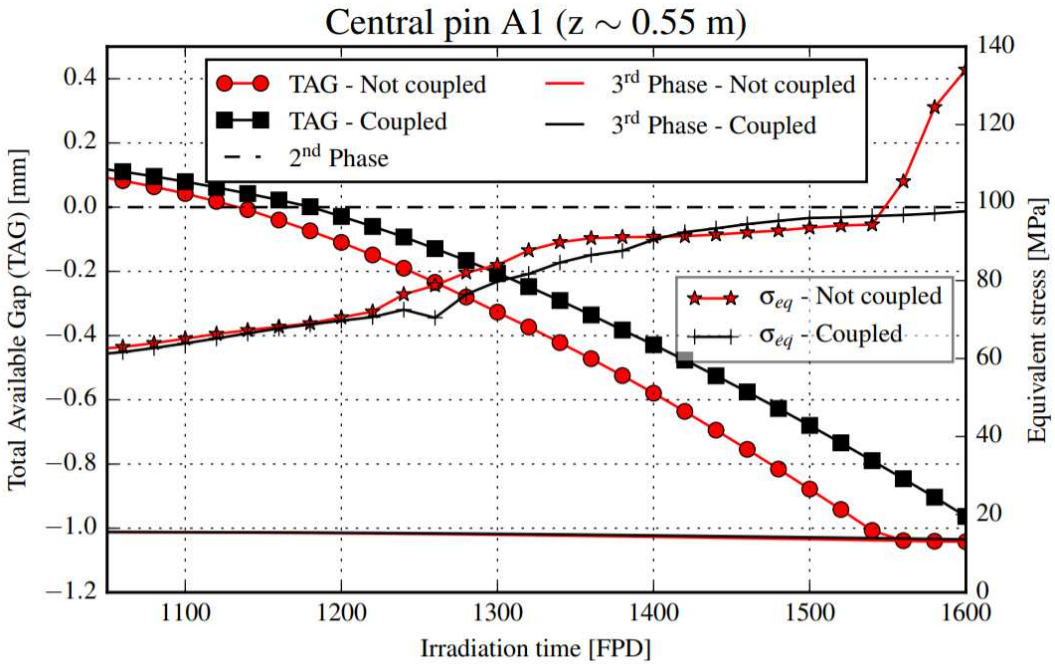

Figure 10: Evolution of the TAG and of the equivalent cladding stress σ_{eq} at the axial position of maximal EOL stress, for the central pin A1. The results obtained with coupled and not coupled simulations are presented, and the TAG limits marking the start of the 2^{nd} and 3^{rd} bundle deformation phases are shown.

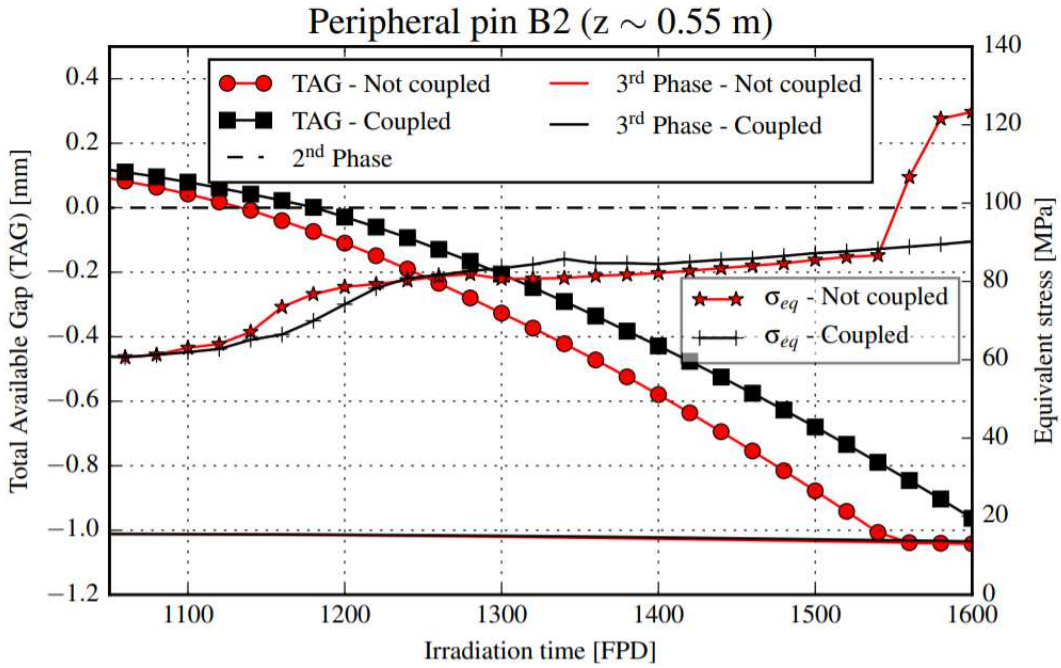

Figure 11: Evolution of the TAG and of the equivalent cladding stress σ_{eq} at the axial position of maximal EOL stress, for the peripheral pin B2. The results obtained with coupled and not coupled simulations are presented, and the TAG limits marking the start of the 2^{nd} and 3^{rd} bundle deformation phases are shown.

4.4 CLADDING TEMPERATURE AND SWELLING GRADIENTS

As evidenced by *Figure 1*, void swelling is strongly temperature dependent, therefore, under the temperature gradients shown in Figure 6, high swelling gradients are stablished within the fuel claddings, which can only be resolved with the 3D thermomechanical model. To illustrate this, the swelling strain profile along the circumference of pin B2 is presented in Figure 12a for an axial position of 0.55 m, where both the swelling strain and its circumferential gradient are maximal. Both the results obtained with the non-coupled and the coupled simulations conducted with the 3D model are presented in the figure. Additionally, in Figure 12b and Figure 12c, the swelling strain distribution within a 1.5-cm-tall axial section of the cladding, at the same axial position, is presented for the non-coupled and coupled simulations, respectively.

As can be observed in Figure 12a, the swelling strain is highly inhomogeneous within the circumference of the cladding. The difference between the maximal and minimal strain represents, in the non-coupled simulation, 40% of its average. As explained before, the temperature gradients are increased in the deformed geometry. Thus, in the coupled simulation, the difference between the maximal and minimal swelling strain within the cladding circumference is larger and represents a 50% of its average.

In Figure 12b and in Figure 12c, a qualitatively similar swelling distribution can be observed within the axial cladding slice in the coupled and in the non-coupled cases. However, the coupling

increases the swelling strain amplitude by 44%. This amplitude is higher than the one computed over a circumferential line (Figure 12a) since the axial temperature gradients induce important axial swelling gradients too. It is worth noting that these axial gradients can only be correctly reproduced if the azimuthal gradients are considered, since the first are strongly "smoothed" out if the cladding temperature is considered homogeneous within its cross section.

Being able to correctly predict the swelling strain distribution is of particular importance, firstly, because it has been shown to produce excessive embrittlement of the cladding's austenitic steel above approximately 2% [7], which motivates the swelling design limit presented in *Table 1*. Additionally, the swelling gradients give place to secondary stresses that, despite generally being relaxed by the irradiation creep [24], could also activate the damaging thermal creep.

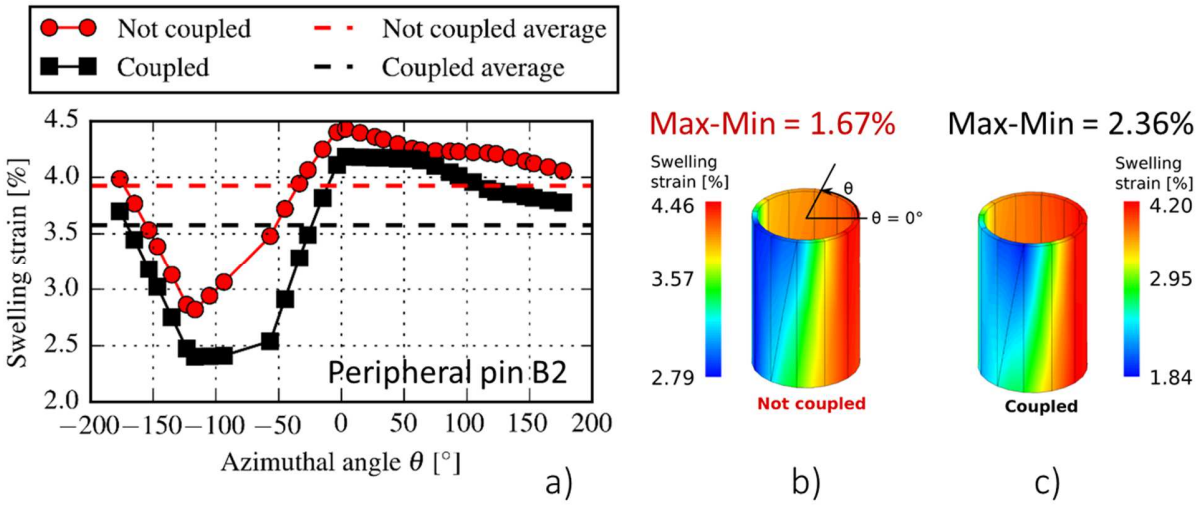

Figure 12: Swelling strain within the cladding circumference of the peripheral pin B2 (a) and within a 1.5-cm-tall axial cladding slice, with (c) and without coupling (b), at an axial position of 0.55 m.

5 TEMPERATURE HISTORY INTERPOLATION

In this section, we compare the results of coupled simulations using the three different temperature interpolation strategies discussed in Section 3.2, namely the *Linear Temperature Increment*, the *Delayed Temperature Increment*, and an interpolation of multiple CFD simulations. The first two methods require doing only one CFD simulation in a deformed geometry per iteration (i.e. per thermomechanical simulation of the irradiation period under consideration). In the third case, 3 CFD simulations on deformed geometries are conducted per iteration. Therefore, two additional CFD simulations are conducted in this case, on partially deformed geometries. In particular, one simulation is conducted in the geometry computed for $t = t_{inc}$ (the incubation time, computed as described in Section 3.2), and the other at $t = \frac{t_{inc}+t_{EOL}}{2}$.

Since the 1D model of DOMAJEUR2 was shown, in Section 4.2, to yield a cladding diametral strain distribution in very good agreement with the prediction of the 3D model, the 1D model was employed for the studies presented in this section. This allowed to increase the number of simulated pins to 19, which is challenging with the 3D model due to is high computational cost. All other geometric parameters of the 7-pin bundle presented in Section 4.1 were conserved, except for the hexcan plate to plate distance that was set to 49.31 mm to accommodate the 19 fuel pins. A 19-pin bundle was selected because its simulation requires significantly less CFD computational time than larger bundles—which are the object of Section 6—, but it allows to evaluate whether the coupling induces the same qualitative effects than the ones observed for the 7-pin bundle or not.

The nominal inlet sodium mass flow rate was set to 2.34 kg/s, as to obtain, like with the 7-pin bundle, an outlet bulk sodium temperature of about 550°C in nominal conditions, considering an inlet temperature of 400°C. The EOL irradiation dose profile presented in Figure 5a was used. Different BOL and EOL linear power profiles were employed—the same for all fuel pins—to account for the fuel burn-up. These profiles are presented in Figure 13a, while a cross section of the CFD mesh—composed of a total of about 6 million cells—is presented in Figure 13b along with the pin naming system employed.

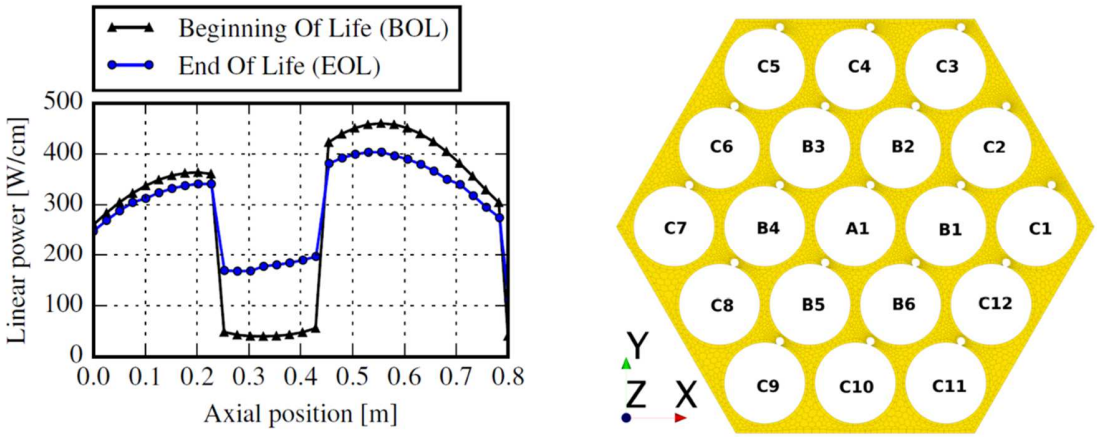

Figure 13: a) BOL and EOL linear power axial profiles used for all the fuel pins of the 19-pin bundle. b) Cross section of the CFD mesh at the outlet of the fuel bundle, where the pin naming system is indicated.

Under these conditions, coupled simulations of the irradiation of the 19-pin bundle were conducted using the three methods for interpolating the temperature distributions to produce the required temperature history for the thermomechanical simulations. The resulting cladding surface temperature evolutions are presented in Figure 14a for 3 different fuel pins, at an altitude z = 0.54 m—where the EOL diametral strain is maximal—, where the evolution in the non-coupled simulation, in which only the power change is considered, is also presented. For each pin and each simulation, the resulting EOL diametral deformation is presented in Figure 14b.

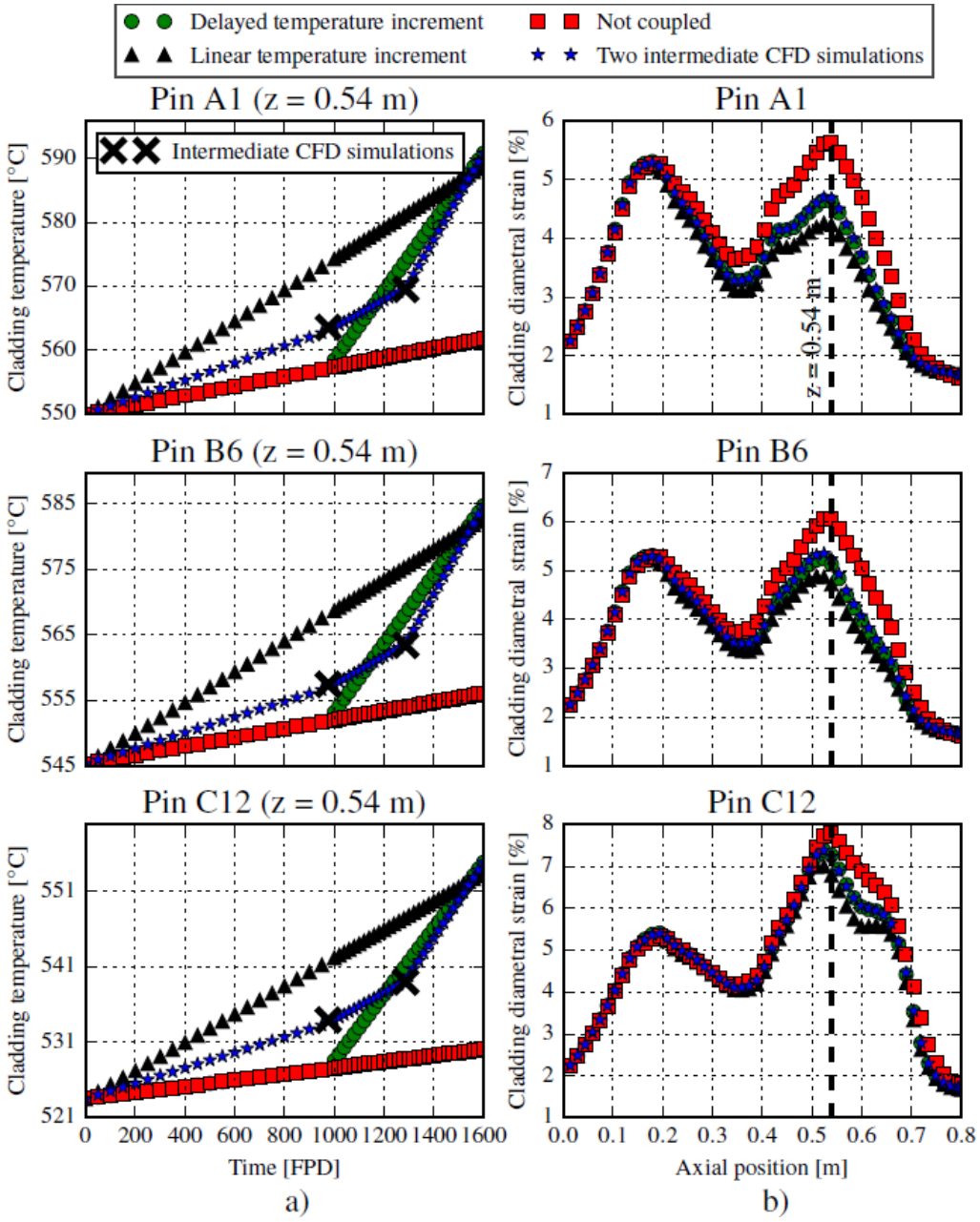

Figure 14: Cladding temperature evolution at z = 0.54 m obtained with the coupled simulations—with two different temperature interpolation methods—, compared to the evolution computed by including two intermediate CFD simulations, and to the results obtained without coupling, for three different fuel pins. b) EOL diametral strain profiles computed in each simulation and for each pin.

It can be noted in Figure 14 that significantly different temperature time evolutions lead to relatively similar EOL diametral deformation profiles, although the effect of considering the delay in the temperature increase caused by the deformation can be observed. All coupled approaches were found to lead to similar maximum cladding temperatures, and they all lead to maximal temperatures highly

superior (~+40°C) to those obtained with the non-coupled approach. The observed effects of the coupling on the cladding temperature evolution and on the cladding EOL diametral strain confirm the trends obtained for the 7-pin fuel bundle.

Additionally, it can be observed in Figure 14a that, at z = 0.54 m and $t = t_{inc} = 976\ FPD$, the CFD simulation yields a cladding temperature only about 5°C higher than the *Delayed Temperature Increment* interpolation, and an even smaller temperature difference is obtained at $t = \frac{t_{inc}+t_{EOL}}{2} = 1287\ FPD$. Consequently, as can be noted in Figure Figure 14b, using two additional CFD calculations in partially deformed geometries to construct the temperature history, employed as input for the thermomechanical simulation, does not have a noticeable impact on the EOL diametral strain of the fuel pins.

In view of these results, the *Delayed Temperature Increment* approach for the computation of the temperature history of the fuel claddings is retained in this work, and it is used in the numerical benchmark presented in Section 6. This approach allows reducing the number of computationally expensive CFD simulations needed for a coupled calculation, by replacing them with appropriate interpolations—based on the computed evolution of the geometry—, without compromising the most relevant results: the EOL deformation of the fuel pins and their EOL temperature distribution.

6 NUMERICAL BENCHMARK

In this section, we present a numerical benchmark based on the simulation of the irradiation of the PFD512 subassembly in the Mk-II core of the experimental SFR Joyo, originally presented in [6]. In that work, the coupling between the subchannel code ASFRE and the bundle thermomechanical code BAMBOO was employed to simulate the irradiation of PFD512, considering the actual PFD512 irradiation period of 327 FPD, as well as a longer 846 FPD irradiation as to evaluate the effects of a high deformation level. Here, we replicate the simulation of the 846 FPD irradiation of PFD512 using the developed coupling between DOMAJEUR2 and STAR-CCM+. The goal of this benchmark exercise is to compare the bundle deformation and temperature distributions computed with the STAR-CCM+/DOMAJEUR2 coupling with the results obtained with ASFRE/BAMBOO.

6.1 BENCHMARK DEFINITION

The main design parameters of the PFD512 subassembly are presented in Table 3, where they are compared to the parameters of the 4th generation SFR [8] used for the 7 and 19 pin bundles presented in the previous sections. The definition of the simulation conditions is based on the data reported in [6], and it is described in what follows.

Parameter	PFD512	4th Generation SFR
Number of fuel pins	127	217

Fuel pin length [m]	1.533	2.136
Heated column length [m]	0.55	0.8
Fuel pin pitch [mm]	6.47	10.8
Fuel pin external diameter [mm]	5.5	9.7
Cladding thickness [mm]	0.5	0.45
Spacer wire diameter [mm]	0.9	1
Spacer wire helix step [mm]	209	180
Hexcan plate to plate distance [mm]	74.7	161.5
Maximum BOL linear power [W/cm]	333	460
BOL sodium mass flow rate [Kg/s]	8.85	27
Inlet sodium temperature [°C]	370	400
Bulk sodium heating rate [°C/m]	327	188

Table 3: Main geometric and thermal-hydraulic characteristics of PFD512, compared to those of a 4th generation SFR.

The linear power profile used for all pins is presented in Figure 15. In order to obtain this power distribution, the power profile reported in [6] for the central pin—also presented in Figure 15—was normalized as to obtain the same total subassembly power of 1.94 MW. We therefore neglect the radial power gradients, reported to be lower than 2%. The non-dimensional distribution of the EOL irradiation dose was assumed to be the same than the non-dimensional linear power distribution, and the maximal EOL irradiation dose reported in [6] was also used here.

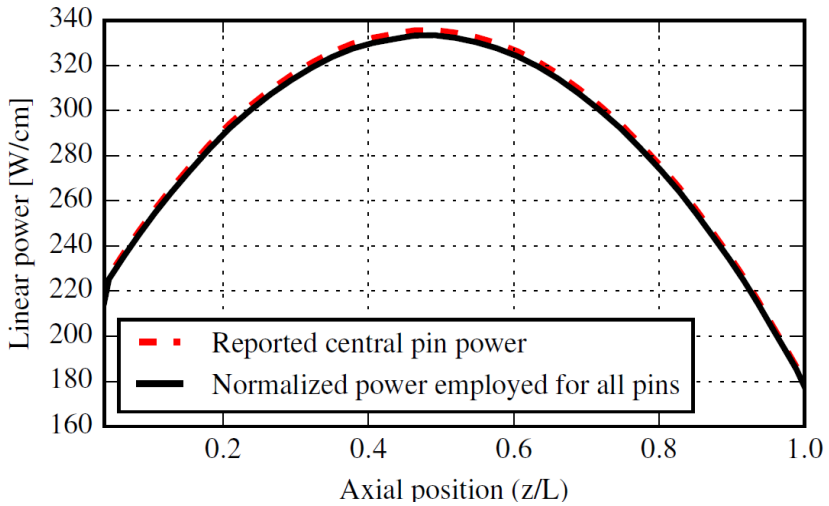

Figure 15: Axial profile of linear power of the highest power fuel pin of PFD512, reported in *[6]*, and normalized profile employed for all fuel pins in the simulations here presented. The axial position z is measured from the base of the heated column, and it is nondimensionalized with the heated column length L.

Even though one of the key aspects of our coupling methodology is the capacity of computing the coolant mass flow rate reduction caused by deformation, we purposely ignore this effect in present benchmark to be able to match the hypothesis made in [6]. Indeed, the authors of that work kept a constant mass flow rate during the irradiation, although they acknowledge that it should vary as the

subassembly is deformed. At the end of Section 6.2, however, the impact of this simplifying hypothesis is investigated.

Finally, the same cladding internal pressure evolution than in [6] was employed here, and the swelling and irradiation creep laws there reported were implemented in DOMAJEUR2 and used for this benchmark.

6.2 BENCHMARK RESULTS

To compare sodium temperature distribution, we consider the subchannels in one of the diagonals of the hexagonal subassembly cross section, as indicated in Figure 16. The average sodium temperatures computed, with a CFD simulation, for each subchannel at the outlet and the midplane (z/L = 0.5) of the heated column, are presented in Figure 17. These results correspond to the non-deformed geometry, and they are there compared with the results presented in [6], computed with the subchannel code ASFRE. The results obtained with the two methods are in general good agreement, although ASFRE predicts an outlet temperature for the central subchannels of about 7°C higher, and outlet temperatures up to 14°C higher in the corner subchannels. A larger temperature difference in the peripheral subchannels, with respect to the CFD results, is in line with the results presented in [18] and [25]. This effect is in part caused by the presence of the spacer wire, which is not explicitly considered in the subchannel simulations.

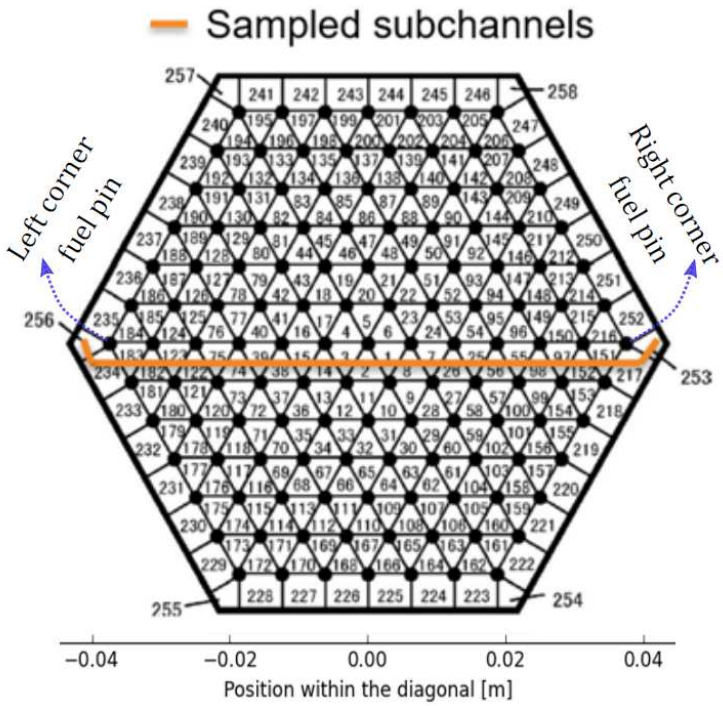

Figure 16: Cross section of PFD512 indicating the subchannels sampled in the CFD simulations. Adapted from [6].

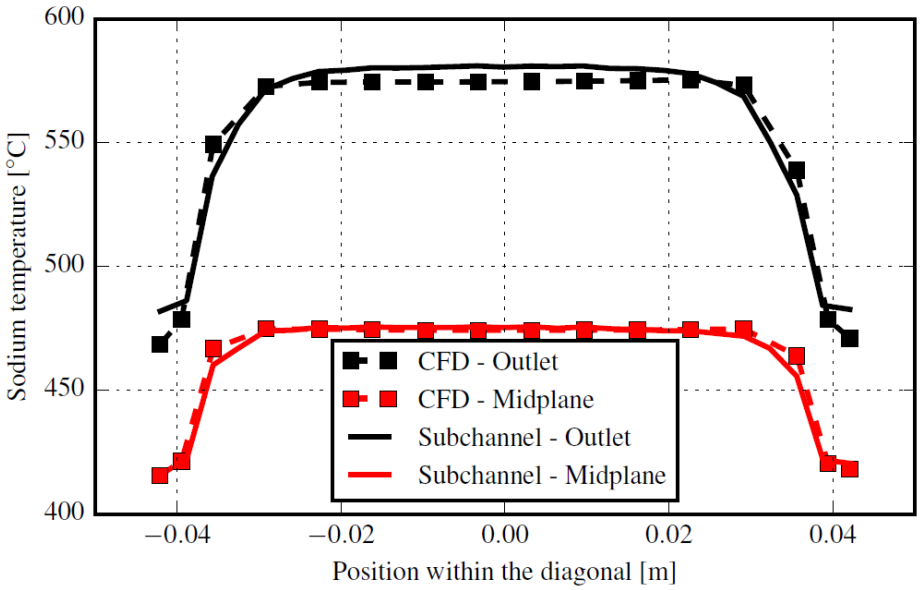

Figure 17: Sodium temperature distribution at the outlet and midplane of the fuel bundle, computed with the subchannel and the CFD simulations in the non-deformed geometry.

The axial profiles of swelling induced and total EOL viscoplastic (swelling and creep) diametral strain of the central pin of PFD512 computed with the STARCCM+/DOMAJEUR2 coupling are presented in Figure 18, where they are compared to the profiles computed by ASFRE/BAMBOO. A very good agreement can be observed between the two simulations, although DOMAJEUR2 (DMJ2 in the figures of this section) computes a slightly higher maximal swelling—and thus total—strain.

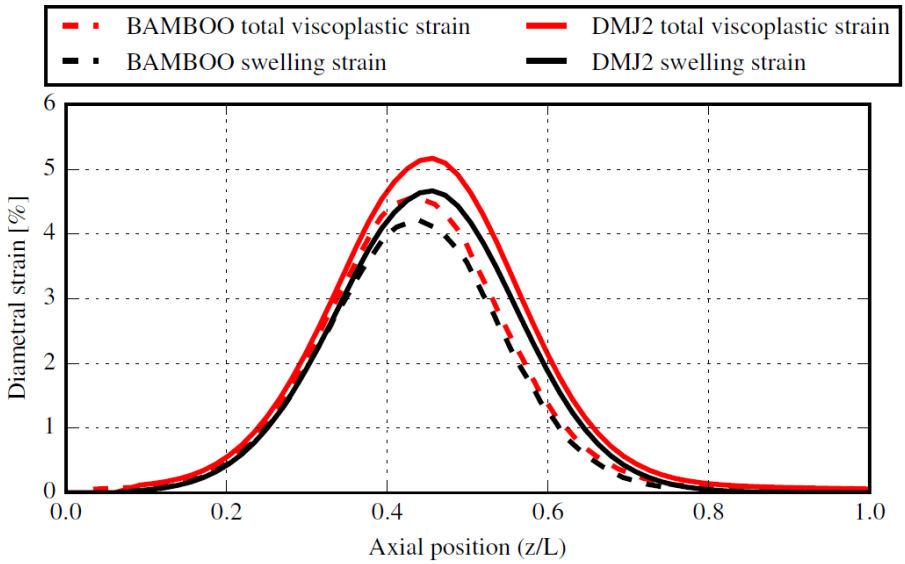

Figure 18: Axial profiles of swelling strain and total viscoplastic diametral strain of the central pin of PFD512, as computed by DOMAJEUR2 and by BAMBOO at EOL.

The EOL axial profile of lateral displacement of the fuel pin presenting the highest helical flexion—the left corner fuel pin that occupies the subchannel N°256 as indicated in Figure 16—computed by DOMAJEUR2 and BAMBOO is presented in Figure 19. It can be there observed that both codes yield a similar pin displacement profile, and that they are in good agreement concerning the position of the maximal deflection and its magnitude.

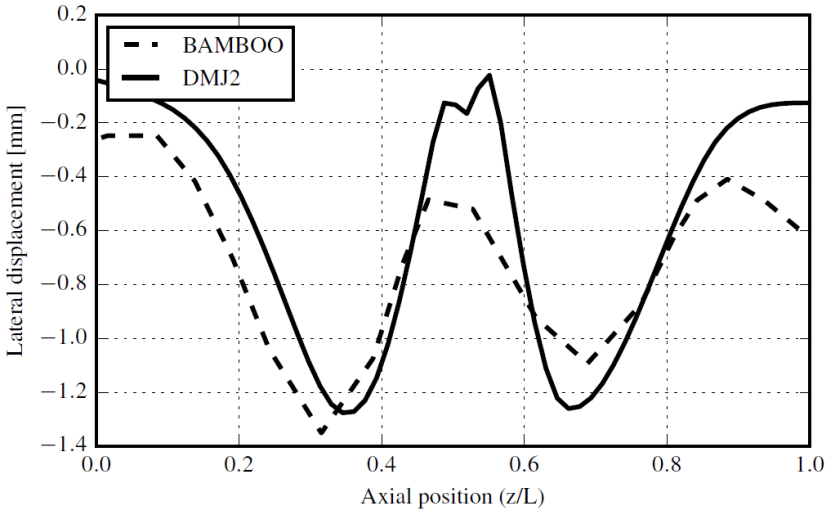

Figure 19: Axial profile of lateral displacement of the left corner pin, computed by BAMBOO and by DOMAJEUR2 at EOL. The displacement is measured over the diagonal indicated in Figure 16, and it is negative towards the left, i.e. towards the hexcan corner in subchannel N°256.

It should be noted that the DOMAJEUR2 results presented so far were obtained without considering the effect of the helical flexion of the pins on their temperature distribution. The helical flexion does noticeably affect the sodium temperature distribution in this case[2], but this temperature change was observed to have a low feedback on the deformation. These effects were local temperature increases in the areas of contact between pins, which appear at a late stage of the irradiation and do not globally affect the geometry of the bundle, and a temperature increase in the periphery of the bundle, which becomes significant close to the end of the heated column. Since the diametral strain of the cladding is extremely low in this region, as can be noted in Figure 18, a potential feedback of a temperature increase in this region is of low importance. However, the coupled simulation here developed allows to explicitly represent the helical flexion of the fuel pins in the CFD simulations, which was done to obtain the temperature distributions presented next.

The outlet sodium temperature computed with the CFD simulation in the EOL deformed geometry are presented in Figure 20, together with the results obtained in the non-deformed geometry, where they are compared with the results obtained with ASFRE. It can be observed that the CFD-computed

[2] Note that the geometry of PFD512 is such—larger wire step and pins of lower diameter—that the lateral displacement of the fuel pins computed at EOL is more than twice the maximum observed in the subassemblies of the PHENIX reactor. Additionally, the sodium heating rate is particularly high (see Table 3), which enhances the local heating caused by the displacement of the fuel pins.

temperature distribution is in good general agreement with that obtained with the subchannel code ASFRE, although differences can be observed mainly in the temperature transition from the center towards the periphery of the bundle. Indeed, on the right side of diagonal, the CFD simulation predicts a more abrupt transition from a high temperature central zone towards a low temperature peripheral zone than the subchannel simulation. The bundle deformation leads to a decrease in the sodium temperature in the center of the bundle, and to a very large temperature increase of about 50°C in the left corner subchannel. Both simulations predict a marked asymmetry in the sodium temperature distribution in the deformed bundle, with the left corner being more than 20°C hotter than the right one. This asymmetry is explained by a higher obstruction of the left corner subchannel.

As in the nominal geometry, the largest temperature differences between the two coupled simulations are observed in the periphery of the bundle, were the spacer wires—explicitly considered only in the CFD simulations—have the largest effect. Indeed, the secondary flow induced by the spacer wires was found to be larger in the corner and edge subchannels, which is in agreement with the findings of [26] and [27]. One of the reasons for this is that, following the length of the bundle, the gap between peripheral pins and the hexcan is always interrupted by the wire in the same angular direction; however, the gaps between fuel pins are interrupted by spacer wires in alternating rotation directions, and thus their effects cancel out partially, as observed by [28]. Being able to correctly capture the complex flow disruptions caused by the spacer wires constitutes a clear advantage of the CFD modelling here implemented with respect to the traditional subchannel approach.

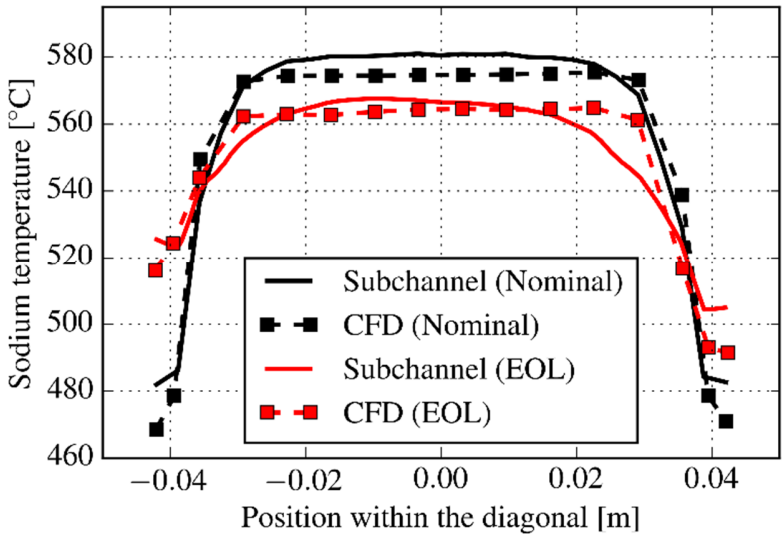

Figure 20: Sodium temperature distribution at the outlet of the fuel bundle, computed with the subchannel and the CFD simulations in the nominal (0 FPD) and EOL (846 FPD) bundles.

In the simulations presented up to now in this section, a constant subassembly mass flow rate was employed, thus neglecting the effects that the deformation has on it in order to match the hypothesis made by [6]. To evaluate these effects, a CFD simulation was conducted in the deformed bundle, using a lower mass flow rate as inlet condition. To do so, the same relative mass flow reduction than that estimated for a 4th generation SFR, for the same average diametral deformation, was considered. Since the Joyo reactor might exhibit a different relationship between mass flow rate and deformation, this simulation should not be understood as a precise quantification of the mass flow rate reduction in Joyo,

but rather as an exploratory exercise to gain insight of the potential consequences a deformation-induced coolant mass flow rate reduction.

The outlet sodium distribution thus obtained is presented in Figure 21, where the distribution obtained in the same geometry without reducing the coolant mass flow rate is included for comparison. It can be there observed that considering the mass flow rate reduction leads to a significant sodium temperature increase in the central region of the bundle, of about 20°C, as opposed to the temperature reduction found in this region when the mass flow reduction is not considered. It also induces a smaller temperature increase in the peripheral subchannels. Then, in this case, the helical flexion has a preponderant role in the periphery of the bundle, while the effect of the mass flow reduction in the central region of the bundle is greater than the effects, in this region, of the mass flow redistribution caused by the helical flexion of the pins. These results highlight the importance of explicitly considering the reduction of the coolant mass flow rate as a consequence of deformation, for which a dedicated model is included in the coupled simulation methodology here presented.

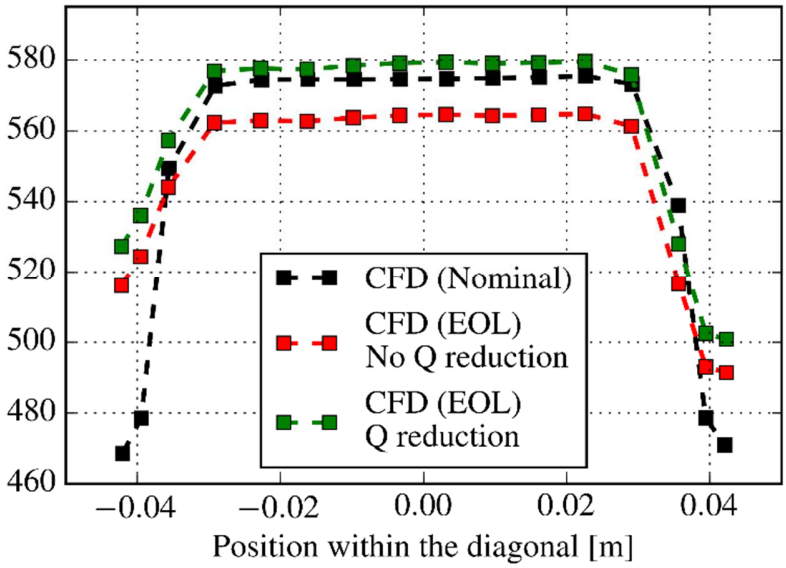

Figure 21: Sodium temperature distribution at the outlet of the fuel bundle, computed with the CFD simulations in the nominal geometry (0 FPD), and in the EOL (846 FPD) deformed bundle with and without sodium mass flow rate reduction.

7 CONCLUSIONS AND PERSPECTIVES

The irradiation of a 7-pin SFR fuel bundle was simulated with a novel coupled thermal-hydraulic/thermomechanical methodology. It was shown that considering the coupling in the numerical simulations leads, for a highly irradiated fuel bundle, to a significant reduction of the void swelling and the irradiation creep of the pin claddings, which are the main contributors to their diametral strain. These variables, averaged over the circumference of the cladding, were in excellent agreement between

a 3D and a beam-based representation of the fuel bundle, which justifies the use of the latter for larger bundle studies thus greatly reducing the computational cost of the numerical simulation.

The computed strain reduction led to a decrease in the contact forces between pins, and thus to a significant reduction of the maximal equivalent stress. This is due to the delay of a phase of bundle mechanical interaction (not allowed during normal operation since it involves a high cladding ovalization), which leads to a sudden increase of the mechanical stresses. Therefore, design margins could be increased by employing the coupled simulation approach.

Additionally, it was shown that considering the high temperature gradients computed with a CFD approach leads to high swelling gradients, which are increased with the coupling. This is relevant due to the swelling induced steel embrittlement and because of the secondary stresses associated to the swelling gradients. In view of these results, the beam-based model was modified to allow considering the azimuthal temperature gradients, and the updated model will be available in the next version of DOMAJEUR2. The high temperature and swelling gradients revealed by the use of the detailed CFD approach suggest that the methodology employed here could be used to determine more accurate material laws, which were established from experiences and simulations without taking neither these gradients nor the coupling effects into account.

The effects of the coupling observed in the 7-pin bundle were also observed in coupled simulations of larger 19-pin bundles. These simulations allowed to evaluate different methods to approximate the history of the cladding temperature distribution during the irradiation based on the interpolation of CFD simulations carried on partially deformed geometries. In particular, an ad-hoc method that allows to reduce the required number of CFD simulations, therefore greatly reducing the computational cost of a coupled simulation, was found to be in excellent agreement with the reference method based on a the interpolation of a larger number of CFD-computed temperature distributions.

Finally, a numerical benchmark against ASFRE-BAMBOO, the state-of-the-art coupled code system for the simulation of SFR subassemblies, was presented. The benchmark, based on the simulation of a highly irradiated 127-pin fuel bundle, showed that the coupled methodology here developed leads to results that are in good agreement with the state-of-the-art code system. However, clear gains were identified from the use of a detailed CFD simulation in our methodology, which allows to capture the complex flow disruptions caused by the spacer wires and by the deformation of the bundle, not correctly captured by the subchannel code ASFRE. Finally, the results also show the importance of using deformation-dependent boundary conditions for the thermal-hydraulic analysis. Indeed, our analysis shows that the fuel assembly coolant mass flow rate model implemented in our coupled methodology (and to our knowledge not considered in other SFR numerical simulation system) is necessary to predict the flow reduction as result of the fuel assembly deformation. This effect induces a sodium temperature increase that could outbalance the effects arising from the geometrical deformation alone.

NOMENCLATURE

$\tilde{\varepsilon}_{Max}^{k-1}(t)$	Approximation of $\varepsilon_{Max}^{k-1}(t)$

$\tilde{T}^k(\boldsymbol{r},t)$	Approximation of $T(\boldsymbol{r},t)$ [°C]
BOL	Beginning Of Life
$T(\boldsymbol{r},t)$	Cladding temperature spatial and time distribution (cladding temperature history) [°C]
CFD	Computational Fluid Dynamics
K	Creep modulus [1/(Pa.dpa)]
α	Creep-swelling coupling coefficient
CDF	Cumulative creep-rupture damage factor
dpa	Displacements Per Atom
EOL	End Of Life
σ_{eq}	Equivalent stress [Pa]
CEA	French Alternative Energies and Atomic Energy Commission
FPD	Full Power Day
$\dot{\varepsilon}_{eq}^{irr.\ creep}$	Irradiation creep equivalent strain rate [1/s]
$\varepsilon_{irr.\ creep}$	Irradiation creep strain
D	Irradiation dose [dpa]
$\varepsilon_{swelling}$	Linear swelling strain
$\varepsilon_{Max,p}^{k-1}(t)$	Maximal creep and swelling induced diametral strain of a fuel pin p
$\boldsymbol{r}$	Position vector [m]
RANS	Reynolds Averaged Navier Stokes
SFR	Sodium-cooled Fast Reactor
$\dot{g_0}$	Stationary swelling rate [1/s]
$\varepsilon_{Max}^{k-1}(t)$	Summation over all fuel pins of theaximal creep and swelling induced diametral strain
Δ_g	Swelling incubation dose [dpa]
δ_g	Swelling transition dose [dpa]
T	Temperature [°C]
$T_{Nom}(\boldsymbol{r},t)$	Temperature distribution in the non-deformed geometry [°C]
T_{cold}	Temperature in the *cold* isothermal state[°C]
t	Time [FPD]
t_{BOL}	Time after 1 FPD of irradiation [FPD]
t_{EOL}	Time at the end of the irradiation period [FPD]
t_{inc}^k	Time from which the effect of the bundle deformation on the temperature distribution is considered, computed in an iteration k
TAG	Total Available Gap
g	Volume swelling
$\dot{g}$	Volume swelling rate [1/dpa]

REFERENCES

[1] K. Katsuyama, T. Nagamine, S. Matsumoto, and M. Ito, “Application of X-Ray Computer Tomography for Observing the Deflection and Displacement of Fuel Pins in an Assembly Irradiated in FBR,” *Journal of Nuclear Science and Technology*, vol. 40, no. 4, pp. 220–226, avril 2003.

[2] E. R. Gilbert and J. F. Bates, “Dependence of irradiation creep on temperature and atom displacements in 20% cold worked type 316 stainless steel,” *Journal of Nuclear Materials*, vol. 65, pp. 204–209, Mar. 1977, doi: 10.1016/0022-3115(77)90057-5.

[3] M. P. Surh, J. B. Sturgeon, and W. G. Wolfer, “Radiation swelling behavior and its dependence on temperature, dose rate, and dislocation structure evolution,” *Journal of Nuclear Materials*, vol. 336, no. 2, pp. 217–224, Feb. 2005, doi: 10.1016/j.jnucmat.2004.09.016.

[4] F. Acosta, T. Cadiou, V. Blanc, and P. Rubiolo, “A new thermal-hydraulics/thermomechanics coupling methodology for the modeling of the behavior of sodium-cooled fast reactors fuel subassemblies under irradiation,” *Nuclear Engineering and Design*, vol. 348, pp. 90–106, Jul. 2019, doi: 10.1016/j.nucengdes.2019.04.014.

[5] “STAR-CCM+ v12.02 User Manual.” 2017.

[6] T. Uwaba, H. Ohshima, and M. Ito, “Analyses of deformation and thermal-hydraulics within a wire-wrapped fuel subassembly in a liquid metal fast reactor by the coupled code system,” *Nuclear Engineering and Design*, vol. 317, pp. 133–145, Jun. 2017, doi: 10.1016/j.nucengdes.2017.03.026.

[7] F. Garner, “Irradiation Performance of Cladding and Structural Steels in Liquid Metal Reactors,” in *Materials Science and Technology*, American Cancer Society, 2006.

[8] T. Beck *et al.*, “Conceptual design of ASTRID fuel sub-assemblies,” *Nuclear Engineering and Design*, vol. 315, pp. 51–60, Apr. 2017, doi: 10.1016/j.nucengdes.2017.02.027.

[9] Gary S. Was, *Fundamentals of Radiation Materials Science. Metals and Alloys*. Berlin: Springer, 2007.

[10] T. Uwaba, M. Ito, and K. Maeda, “Diametral strain of fast reactor MOX fuel pins with austenitic stainless steel cladding irradiated to high burnup,” *Journal of Nuclear Materials*, vol. 416, no. 3, pp. 350–357, Sep. 2011, doi: 10.1016/j.jnucmat.2011.06.033.

[11] T. Uwaba and K. Tanaka, “Development of a Fast Breeder Reactor Fuel Bundle-Duct Interaction Analysis Code—BAMBOO: Analysis Model and Validation by the Out-of-Pile Compression Test,” *Nuclear Technology*, 2001, doi: 10.13182/NT01-A3225.

[12] *INTERNATIONAL ATOMIC ENERGY AGENCY, Structural Materials for Liquid Metal Cooled Fast Reactor Fuel Assemblies-Operational Behaviour, Nuclear Energy Series No. NF-T-4.3, IAEA, Vienna (2012)*.

[13] M. Lainet, B. Michel, J.-C. Dumas, M. Pelletier, and I. Ramière, “GERMINAL, a fuel performance code of the PLEIADES platform to simulate the in-pile behaviour of mixed oxide fuel pins for sodium-cooled fast reactors,” *Journal of Nuclear Materials*, vol. 516, pp. 30–53, Apr. 2019, doi: 10.1016/j.jnucmat.2018.12.030.

[14] D. G. Cacuci, *Handbook of Nuclear Engineering: Vol. 1: Nuclear Engineering Fundamentals; Vol. 2: Reactor Design; Vol. 3: Reactor Analysis; Vol. 4: Reactors of Generations III and IV; Vol. 5: Fuel Cycles, Decommissioning, Waste Disposal and Safeguards*. Springer, 2010.

[7] T. Uwaba, M. Ito, S. Ukai, and M. Pelletier, “Development of a FBR Fuel Bundle-duct Interaction Analysis Code-BAMBOO,” *Journal of Nuclear Science and Technology*, vol. 42, no. 7, pp. 608–617, Jul. 2005.

[16] A. Combescure, A. Hoffman, and P. Pasquet, “The CASTEM Finite Element System,” in *Finite Element Systems*, Berlin: Springer, 1982.

[17] N. Kikuchi, H. Ohshima, M. Tanaka, and A. Hashimoto, “Development of thermal hydraulics analysis code ASFRE for fuel assembly of sodium-cooled fast reactor. Modification of distributed resistance model and validation analysis,” Jun. 2016, Accessed: Sep. 25, 2020. [Online]. Available: http://inis.iaea.org/Search/search.aspx?orig_q=RN:48057379.

[18] T. H. Fanning, W. D. Pointer, and J. W. Thomas, “Multi-resolution modeling of subassembly pin bundles for advanced fast reactor safety simulations,” presented at the International Conference on Mathematics, Computational Methods & Reactor Physics, United States, 2009, [Online]. Available: http://inis.iaea.org/search/search.aspx?orig_q=RN:42064753.

[19] E. Baglietto, J. W. Fricano, and E. Sosnovsky, “CFD Activities in Support of Thermal-hydraulic Modeling of SFR Fuel Bundles,” presented at the The 10th International Topical Meeting on Nuclear Thermal-Hydraulics, Operation and Safety (NUTHOS-10), Japan, Dec. 2014.

[20] T. Cadiou and F. Acosta, “The impact of the fuel pin bundle deformation on the thermal-hydraulics of ASTRID sub-assembly,” presented at the 12th International Topical Meeting on Nuclear Reactor Thermal-Hydraulics, Operation and Safety (NUTHOS-12), Qingdao, China, 2018.

[21] V. S. Mahadevan *et al.*, “High-resolution coupled physics solvers for analysing fine-scale nuclear reactor design problems,” *Philos Trans A Math Phys Eng Sci*, vol. 372, no. 2021, Aug. 2014, doi: 10.1098/rsta.2013.0381.

[22] B. Leturcq, J. B. Minne, and F. Di Paola, “A new structural behavior to perform efficient nonlinear SFR fuel bundle thermomechanical analysis,” presented at the Club Cast3M 2016, 2016, [Online]. Available: http://www-cast3m.cea.fr/index.php?xml=clubcast3m2016.

[23] J. Guidez, *Phenix: le retour d’experience*. EDP Sciences, 2013.

[24] T. Uwaba and S. Ukai, “The secondary stress analyses in the fuel pin cladding due to the swelling gradient across the wall thickness,” *Journal of Nuclear Materials*, vol. 305, no. 1, pp. 21–28, Sep. 2002, doi: 10.1016/S0022-3115(02)00909-1.

[25] X. J. Liu and N. Scarpelli, “Development of a sub-channel code for liquid metal cooled fuel assembly,” *Annals of Nuclear Energy*, vol. 77, pp. 425–435, Mar. 2015, doi: 10.1016/j.anucene.2014.10.030.

[26] J.-H. Jeong, M.-S. Song, and K.-L. Lee, “Thermal-hydraulic effect of wire spacer in a wire-wrapped fuel bundles for SFR,” *Nuclear Engineering and Design*, vol. 320, pp. 28–43, Aug. 2017, doi: 10.1016/j.nucengdes.2017.05.019.

[27] T. Cadiou and A. Saxena, “Thermal–hydraulic numerical simulation of fuel sub-assembly using a dedicated meshing tool,” *Nuclear Engineering and Design*, vol. 295, pp. 162–172, Dec. 2015, doi: 10.1016/j.nucengdes.2015.10.001.

[28] P. Zhao, J. Liu, Z. Ge, X. Wang, and X. Cheng, “CFD analysis of transverse flow in a wire-wrapped hexagonal seven-pin bundle,” *Nuclear Engineering and Design*, vol. 317, pp. 146–157, Jun. 2017, doi: 10.1016/j.nucengdes.2017.03.038.